Available online at www.sciencedirect.com
ScienceDirect
International Journal of Heat and Mass Transfer 51 (2008) 747–756
International Journal of HEAT and MASS TRANSFER
www.elsevier.com/locate/ijhmt

Natural convection flows in a trapezoidal enclosure with uniform and non-uniform heating of bottom wall

E. Natarajan [a], Tanmay Basak [b], S. Roy [a,*]

[a] Department of Mathematics, Indian Institute of Technology Madras, Chennai 600 036, India
[b] Department of Chemical Engineering, Indian Institute of Technology Madras, Chennai 600 036, India

Received 10 August 2006
Available online 27 June 2007

Abstract

A penalty finite element analysis with bi-quadratic elements is performed to investigate the influence of uniform and non-uniform heating of bottom wall on natural convection flows in a trapezoidal cavity. In the present investigation, bottom wall is uniformly and non-uniformly heated while two vertical walls are maintained at constant cold temperature and the top wall is well insulated. Parametric study for the wide range of Rayleigh number (Ra), $10^3 \leqslant Ra \leqslant 10^5$ and Prandtl number (Pr), $0.07 \leqslant Pr \leqslant 100$ shows consistent performance of the present numerical approach to obtain the solutions in terms of stream functions and the temperature profiles. For certain values of the parameters studied in the above range, a symmetry is observed while representing the flow patterns in terms of stream functions. Non-uniform heating of the bottom wall produces greater heat transfer rate at the center of the bottom wall than uniform heating case for all Rayleigh numbers but average Nusselt number shows overall lower heat transfer rate for non-uniform heating case. The power law correlations between average Nusselt number and Rayleigh numbers are presented. The effect of Prandtl number in the variation of local and average Nusselt numbers is more significant for Prandtl numbers in the range 0.07–0.7 than 10–100.

Keywords: Penalty finite element method; Natural convection; Trapezoidal cavity; Uniform and non-uniform heating

1. Introduction

In recent years, an ever-increasing awareness in thermally driven flows reflects that fluid motions and transport processes generated or altered by buoyancy force are of interest due to the practical significances in many fields of science and technology. As a result, this subject is currently studied in diverse areas of meteorology, geophysics, energy storage, fire control, studies of air movement in attics and greenhouses, solar distillers, growth of crystals in liquids, etc. It may also be noted that the sinusoidal wall temperature variation produces uniform melting of materials such as glass as recently reported by Sarris et al. [1] in their detailed study on the effect of sinusoidal top wall temperature variations in a natural convection within a square enclosure where the other walls are insulated. The essential coupling of transport properties of flow and thermal fields leads to an added complexity in buoyancy driven flows. Bejan [2] explains that internal natural convection flow problems are more complex than external ones. Further, Gebhart [3] and Hoogendoorn [4] emphasized various aspects of natural convection flows in a square cavity. External buoyancy driven flow problems are considerably simpler than the internal buoyancy driven flow problems. The physical reason is that at large Rayleigh number classical boundary layer theory yields the same simplifications for external problems, namely, the region exterior to the boundary layer is unaffected by the boundary layer. For

* Corresponding author. Tel.: +91 44 22578492; fax: +91 44 22578470.
E-mail addresses: thillai@iitm.ac.in (E. Natarajan), tanmay@iitm.ac.in (T. Basak), sjroy@iitm.ac.in (S. Roy).

0017-9310/$ - see front matter © 2007 Elsevier Ltd. All rights reserved.
doi:10.1016/j.ijheatmasstransfer.2007.04.027

Nomenclature

g	acceleration due to gravity, m s^{-2}
k	thermal conductivity, W m^{-1} K^{-1}
H	height of the trapezoidal cavity
L	length of the trapezoidal cavity, m
Nu	local Nusselt number
p	pressure
P	dimensionless pressure
Pr	Prandtl number
Ra	Rayleigh number
T	temperature, K
T_h	temperature of hot bottom wall, K
T_c	temperature of cold vertical wall, K
u	x component of velocity
U	x component of dimensionless velocity
v	y component of velocity
V	y component of dimensionless velocity
X	dimensionless distance along x coordinate
Y	dimensionless distance along y coordinate

Greek symbols

α	thermal diffusivity, m^2 s^{-1}
β	volume expansion coefficient, K^{-1}
γ	penalty parameter
θ	dimensionless temperature
ν	kinematic viscosity, m^2 s^{-1}
φ	angle of inclination of the left wall
ρ	density, kg m^{-3}
Φ	basis functions
ψ	stream function
ξ	horizontal coordinate in a trapezoidal
η	vertical coordinate in a trapezoidal

Subscripts

b	bottom wall
s	side wall

confined natural convection, in contrast, boundary layers form near the walls but the region exterior to them is enclosed by the boundary layers and forms a core region. Since the core is partially or fully encircled by the boundary layers, the core flow is not readily determined from the boundary conditions but depend on the boundary layer, which in turn, is influenced by the core. The interactions between the boundary layer and core constitutes a major complexity in the problem and is inherent to all confined convection configurations, namely, that the flow pattern cannot be predicted apriori from the given boundary conditions and geometry. In fact, the situation is even more intricate because it often appears that more than one global core flow is possible and flow subregions, such as cells and layers, may be embedded in the core. This physical complexity in confined convection is not only a topic for analysis but has equal significance for numerical and experimental investigations. The extensive research studies using various numerical simulations reported by Patterson and Imberger [5], Nicolette et al. [6], Hall et al. [7], Hyun and Lee [8], Fusegi et al. [9], Lage and Bejan [10,11] and Xia and Murthy [12] ensure that several attempts have been made to acquire a basic understanding of natural convection flows and heat transfer characteristics in an enclosure.

The majority of works dealing with convection in enclosures is restricted to the cases of simple geometry like rectangular, square, cylindrical and spherical cavities. But the configurations of actual containers occurring in practice is often far from being simple. Iyican and Bayazitoglu [13] investigated natural convective flow and heat transfer within a trapezoidal enclosure with parallel cylindrical top and bottom walls at different temperatures and plane adiabatic side walls. The flow features in trapezoidal enclosures are predicted using data collected for rectangular enclosures. A critical Rayleigh number is presented depending on the tilting angle, where unicellular convection is observed. Karyakin [14] reported two-dimensional laminar natural convection in enclosures of arbitrary cross-section. This study reported on transient natural convection in an isosceles trapezium cavity inclined at angle ϕ to the vertical where a single circulation region is found in the steady state case. The heat transfer rate is found to increase with the increase in the angle ϕ. Perić [15] studied natural convection in a trapezoidal cavities with a series of systematically refined grids from 10×10 to 160×160 control volume and observed the convergence of results for grid independent solutions. Kuyper and Hoogendoorn [16] investigated laminar natural convection flow in trapezoidal enclosures to study the influence of the inclination angle on the flow and also the dependence of the average Nusselt number on the Rayleigh number. Thermosolutal heat transfer within trapezoidal cavity heated at the bottom and cooled at the inclined top part was investigated by Boussaid et al. [17]. The convective heat transport equation was solved by alternating direction implicit (ADI) method combined with a fourth-order compact Hermitian method. It is seen from the literature that no attempt has been made for the detailed calculations of local and average Nusselt numbers on a natural convection flow within a trapezoidal enclosure for various thermal boundary conditions. Therefore as a step towards the eventual developments on natural convection flows within closed enclosures, it is interesting to pursue for a complete understanding of heat transfer rates for many engineering applications such as cooling of computer systems and other electronic equipments.

The present study deals with a natural convection flow within a trapezoidal enclosure where the bottom wall is heated (uniformly and non-uniformly) and vertical walls are cooled by means of a constant temperature bath whereas the top wall is well insulated. The consistent penalty finite element method [18] has been used to solve the nonlinear coupled partial differential equations for flow and temperature fields with both uniform and non-uniform temperature distributions prescribed at the bottom wall.

2. Mathematical formulation

Consider a trapezoidal cavity of length L and height H with the left wall inclined at an angle $\varphi = 30^\circ$ with the y-axis. The velocity boundary conditions are assumed to be no-slip on solid boundaries. The fluid is assumed to be incompressible, Newtonian and laminar. For the treatment of the buoyancy term in the momentum equation, Boussinesq approximation is adopted to account for the variations of temperature as a function of density, and to couple in this way the temperature field to the flow field. The governing equations for steady natural convection flow using conservation of mass, momentum and energy can be written as

$$\frac{\partial u}{\partial x}+\frac{\partial v}{\partial y}=0, \tag{1}$$

$$u\frac{\partial u}{\partial x}+v\frac{\partial u}{\partial y}=-\frac{1}{\rho}\frac{\partial p}{\partial x}+\nu\left(\frac{\partial^2 u}{\partial x^2}+\frac{\partial^2 u}{\partial y^2}\right), \tag{2}$$

$$u\frac{\partial v}{\partial x}+v\frac{\partial v}{\partial y}=-\frac{1}{\rho}\frac{\partial p}{\partial y}+\nu\left(\frac{\partial^2 v}{\partial x^2}+\frac{\partial^2 v}{\partial y^2}\right)+g\beta(T-T_c), \tag{3}$$

$$u\frac{\partial T}{\partial x}+v\frac{\partial T}{\partial y}=\alpha\left(\frac{\partial^2 T}{\partial x^2}+\frac{\partial^2 T}{\partial y^2}\right). \tag{4}$$

The boundary conditions are as follows:

At the bottom wall,

$$u=0,\quad v=0,\quad T=T_h\quad\text{or}\quad T=(T_h-T_c)\sin\left(\frac{\pi x}{L}\right)+T_c,$$

at the left and right vertical walls,

$$u=0,\quad v=0,\quad T=T_c \tag{5}$$

and at the top wall

$$u=0,\quad v=0,\quad \frac{\partial T}{\partial y}=0.$$

Using the following transformation of variables:

$$X=\frac{x}{H},\quad Y=\frac{y}{H},\quad U=\frac{uH}{\alpha},\quad V=\frac{vH}{\alpha},$$
$$P=\frac{pH^2}{\rho\alpha^2},\quad \theta=\frac{T-T_c}{T_h-T_c}. \tag{6}$$

The governing equations (1)–(4) reduce to non-dimensional form:

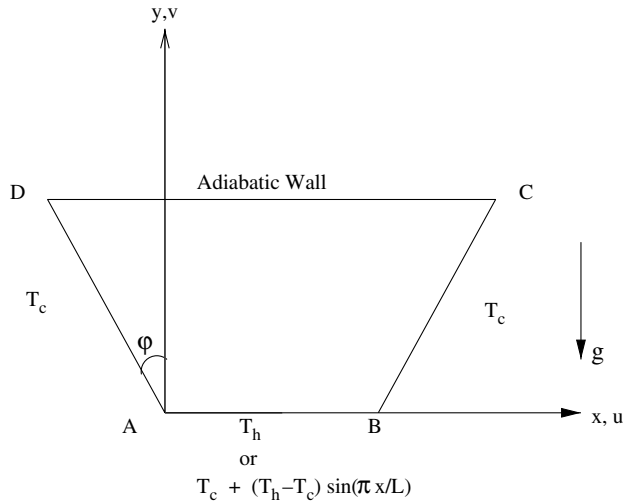

Fig. 1. Schematic diagram of the physical system.

$$\frac{\partial U}{\partial X}+\frac{\partial V}{\partial Y}=0, \tag{7}$$

$$U\frac{\partial U}{\partial X}+V\frac{\partial U}{\partial Y}=-\frac{\partial P}{\partial X}+Pr\left(\frac{\partial^2 U}{\partial X^2}+\frac{\partial^2 U}{\partial Y^2}\right), \tag{8}$$

$$U\frac{\partial V}{\partial X}+V\frac{\partial V}{\partial Y}=-\frac{\partial P}{\partial Y}+Pr\left(\frac{\partial^2 V}{\partial X^2}+\frac{\partial^2 V}{\partial Y^2}\right)+Ra\,Pr\,\theta, \tag{9}$$

$$U\frac{\partial \theta}{\partial X}+V\frac{\partial \theta}{\partial Y}=\frac{\partial^2 \theta}{\partial X^2}+\frac{\partial^2 \theta}{\partial Y^2} \tag{10}$$

with the boundary conditions (see Fig. 1)

$$\begin{aligned}&U=0,\quad V=0,\quad \theta=1\quad\text{or}\quad \theta=\sin(\pi X)\quad\text{on } AB,\\ &U=0,\quad V=0,\quad \theta=0\quad\text{on } AD,\ BC,\\ &U=0,\quad V=0,\quad \frac{\partial\theta}{\partial Y}=0\quad\text{on } CD.\end{aligned} \tag{11}$$

3. Solution procedure and post-processing

The momentum and energy balance equations (8)–(10) are solved using the Galerkin finite element method. The continuity equation (7) will be used as a constraint due to mass conservation and this constraint may be used to obtain the pressure distribution [18–20]. In order to solve Eqs. (8) and (9), we use the penalty finite element method where the pressure P is eliminated by a penalty parameter γ and the incompressibility criteria given by Eq. (7) (see Reddy [18]) which results in

$$P=-\gamma\left(\frac{\partial U}{\partial X}+\frac{\partial V}{\partial Y}\right). \tag{12}$$

The continuity equation (7) is automatically satisfied for large values of γ. Typical value of γ that yield consistent solutions is 10^7 [18–20].

Using Eq. (12), the momentum balance equations (8) and (9) reduce to

$$U\frac{\partial U}{\partial X}+V\frac{\partial U}{\partial Y}=\gamma\frac{\partial}{\partial X}\left(\frac{\partial U}{\partial X}+\frac{\partial V}{\partial Y}\right)+Pr\left(\frac{\partial^2 U}{\partial X^2}+\frac{\partial^2 U}{\partial Y^2}\right) \tag{13}$$

and

$$U\frac{\partial V}{\partial X}+V\frac{\partial V}{\partial Y}=\gamma\frac{\partial}{\partial Y}\left(\frac{\partial U}{\partial X}+\frac{\partial V}{\partial Y}\right)+Pr\left(\frac{\partial^2 V}{\partial X^2}+\frac{\partial^2 V}{\partial Y^2}\right)+RaPr\theta \tag{14}$$

The system of Eqs. (10), (13) and (14) with boundary conditions Eq. (11) is solved by using Galerkin finite element method. Since the solution procedure is explained in earlier works [19,20], the detailed description is not included in this paper. The numerical solutions are obtained in terms of the velocity components (U, V) and stream function (ψ) is evaluated using the relationship between the stream function (ψ) and the velocity components [21], where the stream function (ψ) is defined in the usual way as $U=\frac{\partial\psi}{\partial Y}$ and $V=-\frac{\partial\psi}{\partial X}$. It may be noted that the positive sign of ψ denotes anti-clockwise circulation and the clockwise circulation is represented by the negative sign of ψ. The no-slip condition is valid at all boundaries as there is no cross flow, hence $\psi=0$ is used for the boundaries. The heat transfer coefficient in terms of the local Nusselt number (Nu) is defined by

$$Nu=-\frac{\partial\theta}{\partial n}, \tag{15}$$

where n denotes the normal direction on a plane.

The local Nusselt numbers at bottom wall (Nu_b), left wall (Nu_l) and right wall (Nu_r) are defined as

$$Nu_b=-\sum_{i=1}^{9}\theta_i\frac{\partial\Phi_i}{\partial Y}, \tag{16}$$

$$Nu_l=-\sum_{i=1}^{9}\theta_i\left(\cos\varphi\frac{\partial\Phi_i}{\partial X}+\sin\varphi\frac{\partial\Phi_i}{\partial Y}\right) \tag{17}$$

and

$$Nu_r=-\sum_{i=1}^{9}\theta_i\left(\cos\varphi\frac{\partial\Phi_i}{\partial X}-\sin\varphi\frac{\partial\Phi_i}{\partial Y}\right). \tag{18}$$

Note that, $\varphi=30^\circ$ for the present work. The average Nusselt numbers at the bottom, left and right walls are

$$\overline{Nu_b}=\frac{\int_0^1 Nu_b\,dX}{X|_0^1}=\int_0^1 Nu_b\,dX, \tag{19}$$

$$\overline{Nu_l}=\cos\varphi\int_0^{\frac{1}{\cos\varphi}}Nu_l\,ds_1 \tag{20}$$

and

$$\overline{Nu_r}=\cos\varphi\int_0^{\frac{1}{\cos\varphi}}Nu_r\,ds_2, \tag{21}$$

where ds_1 and ds_2 are small elemental length along the left and right walls, respectively.

4. Results and discussion

4.1. Numerical tests

The computational domain consists of 20×20 bi-quadratic elements which correspond to 41×41 grid points in ξ–η domain and an overview of grid generation is discussed in Appendix-A. The bi-quadratic elements with lesser number of nodes smoothly capture the non-linear variations of the field variables which are in contrast with finite difference/finite volume solutions available in the literature [15,16]. Numerical solutions are obtained for various values of $Ra=10^3$–10^5 and $Pr=0.07$–100 with uniform and non-uniform heating of the bottom wall where the two vertical walls are cooled and the top wall is well insulated. The jump discontinuities in Dirichlet type of wall boundary conditions at the corner points (see Fig. 1) correspond to computational singularity. To ensure the convergence of the numerical solution to the exact solution, the grid sizes have been optimized and the results presented here are independent of grid sizes. In particular, the singularity at the corner nodes of the bottom wall needs special attention. The grid size dependent effect of the temperature discontinuity at the corner points upon the local (and the overall) Nusselt numbers tend to increase as the mesh spacing at the corner is reduced. One of the ways for handling the problem is assuming the average temperature of the two walls at the corner and keeping the adjacent grid-nodes at the respective wall temperatures. Alternatively, based on earlier work by Ganzarolli and Milanez [22], this procedure is still grid dependent unless a sufficiently refined mesh is implemented. Accordingly, once any corner formed by the intersection of two differently heated boundary walls is assumed at the average temperature of the adjacent walls, the optimal grid size obtained for each configuration corresponds to the mesh spacing over which further grid refinements lead to grid invariant results in both heat transfer rates and flow fields. Similar observations are also reported in an earlier work by Corcione [23].

The stream functions and temperature contours have been compared with finite volume based solutions [16] and the solutions are in well agreement. It may be noted that current solution is based on 20×20 bi-quadratic element whereas the earlier work [16] is based on 60×60 control volume grid. In the current investigation, Gaussian quadrature based finite element method provides the smooth solutions at the interior domain including the corner regions as evaluation of residual depends on interior Gauss points and thus the effect of corner nodes are less pronounced in the final solution. In general, the Nusselt numbers for finite difference/finite volume based methods are calculated at any surface using some interpolation functions [15,16] which are now avoided in the current work. The present finite element approach offers special advantage on evaluation of local Nusselt number at the bottom and side walls as the element basis functions are used to evaluate the heat flux.

Flow and temperature fields are shown in terms of streamlines and isotherms, respectively. Owing to the symmetrical boundary conditions on the vertical walls, the flow and temperature fields are symmetrical about the mid-length of the enclosure. The symmetrical boundary conditions in the vertical direction result in a pair of counter-rotating cells in the left and right halves of the enclosure for all the parametric values considered. Therefore, the flows in the left and right halves of the enclosure are identical except for the sense of rotation. Each cell ascends along the symmetry axis, then faces the upper adiabatic wall through which it moves horizontally towards the corresponding cold wall and finally it descends along the corresponding cold wall under the effect of cooling.

4.2. Effects of Rayleigh number: uniform heating at bottom wall

Figs. 2–5 illustrate the stream function and isotherm contours of the numerical results for various $Ra = 10^3$–10^5 and $Pr = 0.07$–10 when the bottom wall is uniformly heated and the side walls are cooled while the top wall is well insulated. As expected due to the cold vertical walls, fluids rise up from middle portion of the bottom wall and flow down along the two vertical walls forming two symmetric rolls with clockwise and anti-clockwise rotations inside the cavity. At $Ra = 10^3$, the magnitudes of stream function are considerably lower and the heat transfer is purely due to conduction (figure not shown). During conduction dominant heat transfer, the temperature contours with $\theta = 0.05$–0.3 occur symmetrically near the side walls of the enclosure. The other temperature contours with $\theta \geqslant 0.4$ are smooth curves symmetric with respect to the vertical symmetric line. The conduction dominant heat transfer will be illustrated later via average Nusselt number vs Rayleigh number plot and the critical Rayleigh number would indicate the initiation of the significant effect of convective heat transfer.

During conduction dominant heat transfer, the temperature profiles are almost invariant w.r.t. Ra, and it is observed that the significant convection is initiated at $Ra = 5 \times 10^3$ with $Pr = 0.07$. At $Ra = 5 \times 10^3$ (Fig. 2), the distortion of the isotherms increases gradually and the advection takes the command, becoming the dominant mode of heat transfer. The circulations are greater near the center and least at the wall due to no-slip boundary conditions. Due to initiation of convection, the isotherms are significantly distorted and pushed near the vertical walls and it is observed that isotherm with $\theta = 0.4$ breaks into two symmetric contour lines. At the small Rayleigh number ($Ra = 5 \times 10^3$) except near the wall, the stream functions are almost circular. As Rayleigh number

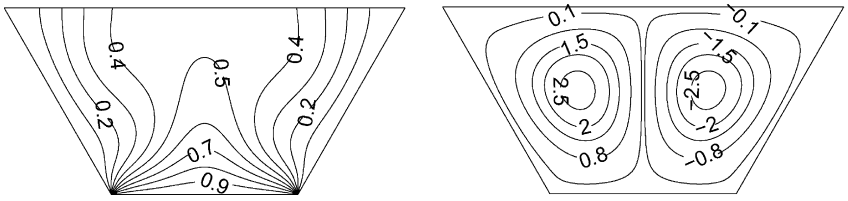

Fig. 2. Temperature and stream function contours for uniform bottom heating, $\theta(X,0) = 1$, with $Pr = 0.07$ and $Ra = 5 \times 10^3$. Clockwise and anti-clockwise flows are shown via negative and positive signs of stream functions, respectively.

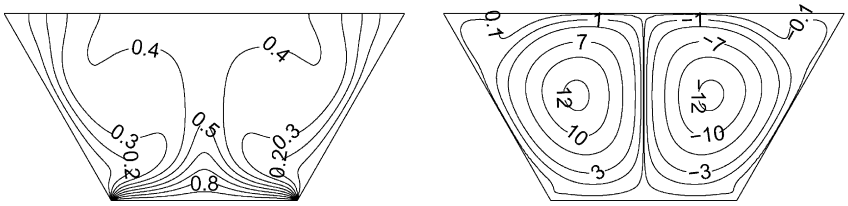

Fig. 3. Temperature and stream function contours for uniform bottom heating, $\theta(X,0) = 1$, with $Pr = 0.07$ and $Ra = 10^5$. Clockwise and anti-clockwise flows are shown via negative and positive signs of stream functions, respectively.

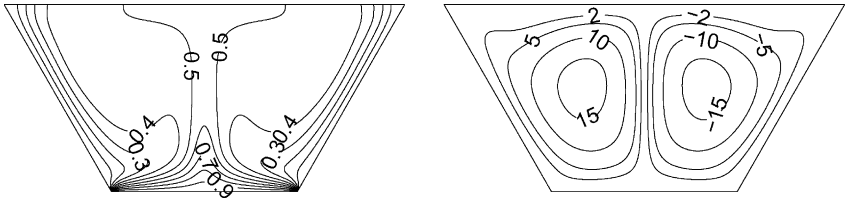

Fig. 4. Temperature and stream function contours for uniform bottom heating, $\theta(X,0) = 1$, with $Pr = 0.7$ and $Ra = 10^5$. Clockwise and anti-clockwise flows are shown via negative and positive signs of stream functions, respectively.

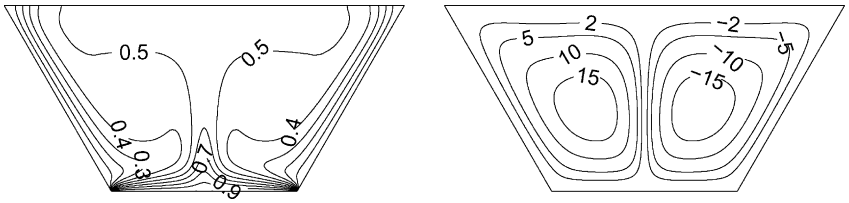

Fig. 5. Temperature and stream function contours for uniform bottom heating, $\theta(X,0)=1$, with $Pr=10$ and $Ra=10^5$. Clockwise and anti-clockwise flows are shown via negative and positive signs of stream functions, respectively.

increases to $Ra=10^5$, the buoyancy driven circulation inside the cavity also increases as seen from greater magnitudes of the stream functions (Fig. 3). It is interesting to observe that the stream function contours near the walls tend to have neck formation due to stronger circulation at higher Ra which contrasts the circulation patterns at smaller Ra as seen in Fig. 2. Due to stronger circulation, the isotherms are compressed near the middle portion of the vertical walls. Consequently, at $Ra=10^5$, the temperature gradients near both the bottom and side walls tend to be significant to develop the thermal boundary layer. Due to greater circulation near the central core at the top half of the enclosure, there are small gradients in temperature at the central regime whereas a large stratification zone of temperature is observed at the vertical symmetry line due to stagnation of flow. The thermal boundary layer develops partially within the cavity for $Ra=10^3$ whereas for $Ra=10^5$, the isotherms presented in Fig. 3 indicate that the thermal boundary layer develops almost throughout the entire cavity.

Comparative studies in Figs. 3–5 show that as Pr increases from 0.07 to 10, the values of stream function and isotherms in the core cavity increase. For $Pr=0.07$ the streamlines look almost circular at the central regime, circular streamline pattern gradually gets deformed for $Pr=0.7$ and finally for $Pr=10$, the streamlines near the walls and the core tend to take the shape of the cavity signifying the increasing intensity of circulations. In addition, at higher Ra, the temperature contours ($\theta \leqslant 0.4$) are compressed towards the vertical side and the compression of isotherm contours still continues and the compression is more for $Pr=0.7$ and 10. Note that, the temperature varies with $\theta=0.4$–0.5 for $Pr=0.7$ (Fig. 4) near the central core regime at the top half of the enclosure whereas the temperature varies within $\theta=0.5$–0.6 for $Pr=10$ as seen in Fig. 5. Due to greater circulation at $Pr=10$, the zone of stratification of temperature at the central symmetric line is reduced.

4.3. Effects of Rayleigh number: non-uniform heating at bottom wall

Stream function and isotherm contours are displayed in Figs. 6–8 for $Ra=10^5$ and $Pr=0.07$–10 when the bottom wall is non-uniformly heated and the side walls are cooled while the top wall is well insulated. As seen in Figs. 2–5, uniform heating of the bottom wall causes a finite discontinuity in Dirichlet type of boundary conditions for the temperature distribution at the edges of the bottom wall. In contrast, the non-uniform heating removes the singularities at the edges of the bottom wall and provides a smooth temperature distribution in the entire cavity. Due to the non-uniform heating of the bottom wall for $Ra=10^3$ and

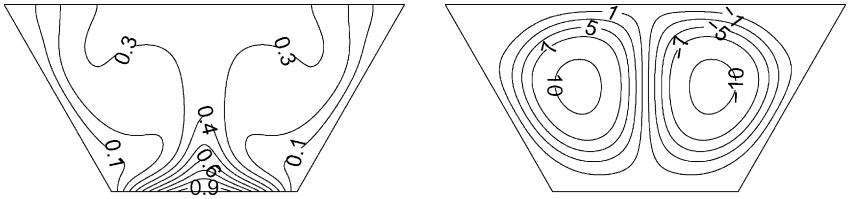

Fig. 6. Temperature and stream function contours for non-uniform bottom heating, $\theta(X,0)=\sin(\pi X)$, with $Pr=0.07$ and $Ra=10^5$. Clockwise and anti-clockwise flows are shown via negative and positive signs of stream functions, respectively.

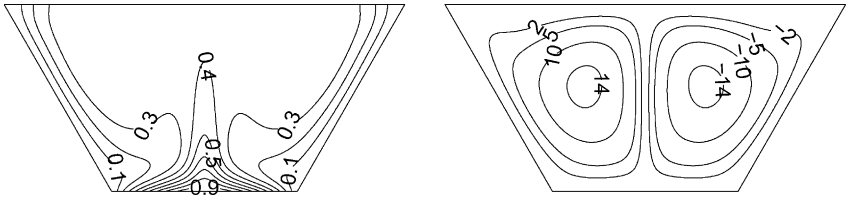

Fig. 7. Temperature and stream function contours for non-uniform bottom heating, $\theta(X,0)=\sin(\pi X)$, with $Pr=0.7$ and $Ra=10^5$. Clockwise and anti-clockwise flows are shown via negative and positive signs of stream functions, respectively.

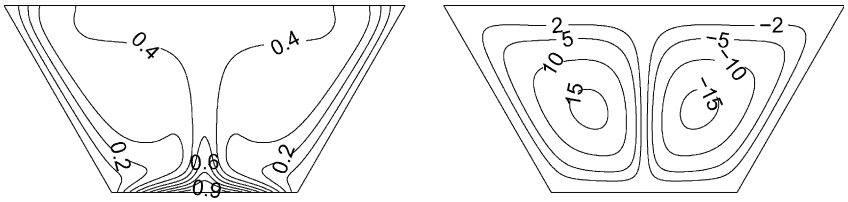

Fig. 8. Temperature and stream function contours for non-uniform bottom heating, $\theta(X,0) = \sin(\pi X)$, with $Pr = 10$ and $Ra = 10^5$. Clockwise and anti-clockwise flows are shown via negative and positive signs of stream functions, respectively.

$Pr = 0.07$, the development of thermal boundary layer is less as compared to the uniform heating case within the cavity (figure not shown). For $Pr = 0.07$ the conduction dominant heat transfer mode is observed up to $Ra = 3 \times 10^3$ (figure not shown) which is in contrast with the uniform heating case where the critical Rayleigh number is around 5×10^3. Note that, the temperature at the bottom wall is non-uniform and maxima in temperature occurs at the center. Therefore, the greater heat transfer rate will occur at the center and the detailed analysis will be illustrated in the next section.

The circulation pattern is qualitatively similar to the uniform heating case with the identical situation (Fig. 6). Due to non-uniform bottom heating, the heating rate near the wall is generally lower which induces less buoyancy effect resulting in less thermal gradient throughout the domain. The uniformity in temperature distribution and least temperature gradients are still observed at the central core regime within the top half of the domain. The less buoyancy effect also leads to a large zone of stratification of temperature at the vertical line of symmetry (Fig. 6). The effect of Prandtl number is also pronounced for $Ra = 10^5$ as seen in Figs. 6–8 where the greater circulation causes more heat to be distributed in the central regime. Similar to the uniform heating case, the streamline contours near the walls tend to take the shape of the cavity at $Pr = 0.7$ and 10 (Figs. 7 and 8). However, compared to uniform heating cases, the values of temperature contours are less near the central and top portion of the enclosure for non-uniform heating case. The greater values of temperature contours are highly densed near the bottom wall which may indicate a lower heating rates at the top as well as central regime of the enclosure.

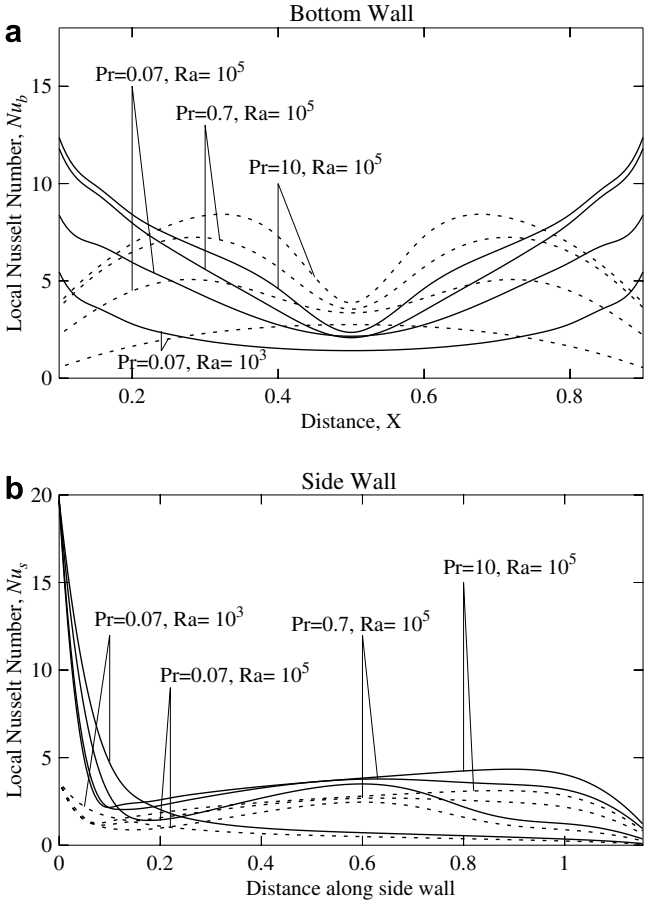

Fig. 9. Variation of local Nusselt number with distance (a) at the bottom wall (b) at the side wall for uniform heating (—) and non-uniform heating (---).

4.4. Heat transfer rates: local and average Nusselt numbers

Fig. 9 displays the effects of Ra and Pr on the local Nusselt numbers at the bottom and side walls (Nu_b, Nu_s). As a result of symmetry in the temperature field, heat transfer is symmetrical with respect to midlength ($X = 1/2$). For uniform heating of the bottom wall, the heat transfer rate decreases from the left of the bottom wall and attains its minimum value at the center $X = 1/2$ and then increases towards the right edge of the bottom wall (Fig. 9a). On the contrary, for non-uniformly heated bottom wall, Nu_b increases from the left edge of the bottom wall, attains its maximum value near the center at lower Ra. Local Nusselt number increases with Ra due to stronger fluid circulation. Further at $Ra = 10^5$, non-uniform heating produces a sinusoidal type of local heat transfer rate symmetrical with respect to mid-length $X = 1/2$. The physical reason of this type of behavior is due to the higher values of stream function (i.e., high flow rate) occur in the middles of the first and second half of the cavity. As Pr increases from 0.07 to 10, the local Nusselt number at the bottom wall increases as seen in Fig. 9a. The temperature contours diverge from the corner points towards the central vertical line for uniform heating cases and therefore local Nusselt number is a monotonically decreasing function with the

distance. In contrast, for non-uniform heating cases the temperature contours are compressed around the intermediate zones between corner and the vertical line of symmetry, and local Nusselt number is maximum at around X = 0.3 and 0.7.

Fig. 9b illustrates the heat transfer rate at the side wall. Due to the symmetry in the boundary condition, the local Nusselt number is identical along both the side walls. The local Nusselt number (Nu_s) is found to decrease with vertical distance along the cold side wall for $Ra = 10^3$ with $Pr = 0.07$ in both uniform and non-uniform heating cases. It is interesting to note that, the heat transfer rate initially decreases and later increases with distance for $Ra = 10^5$ with $Pr = 0.7$ and 10. This is due to the fact that, at higher Ra, the isotherms are largely condensed near the middle portion of the side wall due to stronger circulation and the thermal gradient is less near the bottom corner point due to less circulation. In addition, the temperature contours are compressed towards the side walls away from the corner points at the bottom. Therefore, the heat fluxes are enhanced at the regimes away from bottom corner points. The heat transfer rates are qualitatively similar, but reduced for non-uniform bottom wall heating cases as compared to the uniform heating case.

The overall effects upon the heat transfer rates are displayed in Fig. 10a–d, where the distributions of the average Nusselt number of bottom and side walls, are plotted vs the logarithmic Rayleigh number. The average Nusselt numbers are obtained using Eqs. (19)–(21) where the integral is evaluated using Simpson's 1/3 rule. Note that, Fig. 10a and b (Cases a and b) illustrates uniform heating case and Fig. 10(c) and (d) (Cases c and d) illustrates non-uniform heating case. The values of the average Nusselt numbers along the side walls are less compared to the bottom wall. This is due to the fact that the rate of heat transfer to the fluid from the bottom wall is more compared to the side wall. The average Nusselt numbers for both bottom and side walls remain constant up to $Ra = 5 \times 10^3$ for uniform heating cases whereas up to $Ra = 3 \times 10^3$ for non-uniform heating cases. The influence of the Rayleigh number on the Nusselt number becomes significant at higher Rayleigh number. The average Nusselt number at the bottom and sidewalls were thermally balanced within 3% error. The values of average Nusselt number is more in the case of uniform heating compared to non-uniform heating as seen in Fig. 10a–d. The insets show the log–log plot for average Nusselt number vs Rayleigh number for convection dominant regimes. The log–log linear plot

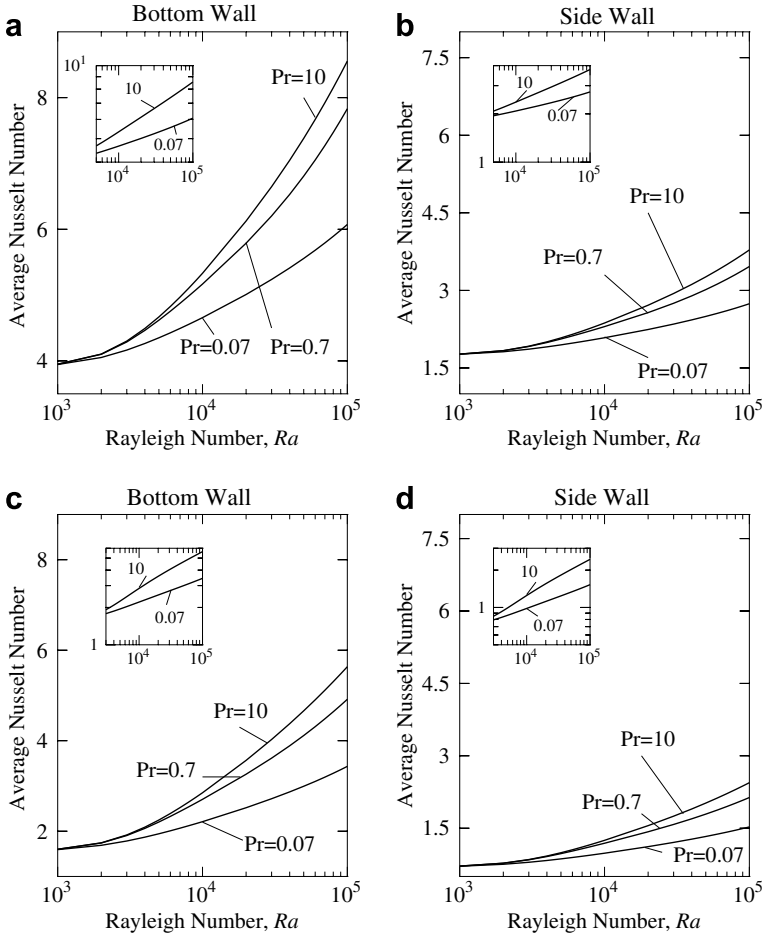

Fig. 10. Variation of average Nusselt number with Rayleigh number for uniform heating [(a) and (b)] and non-uniform heating [(c) and (d)]. The insets show the loglog plot of average Nusselt number vs. Rayleigh number for $Pr = 0.07$ and 10.

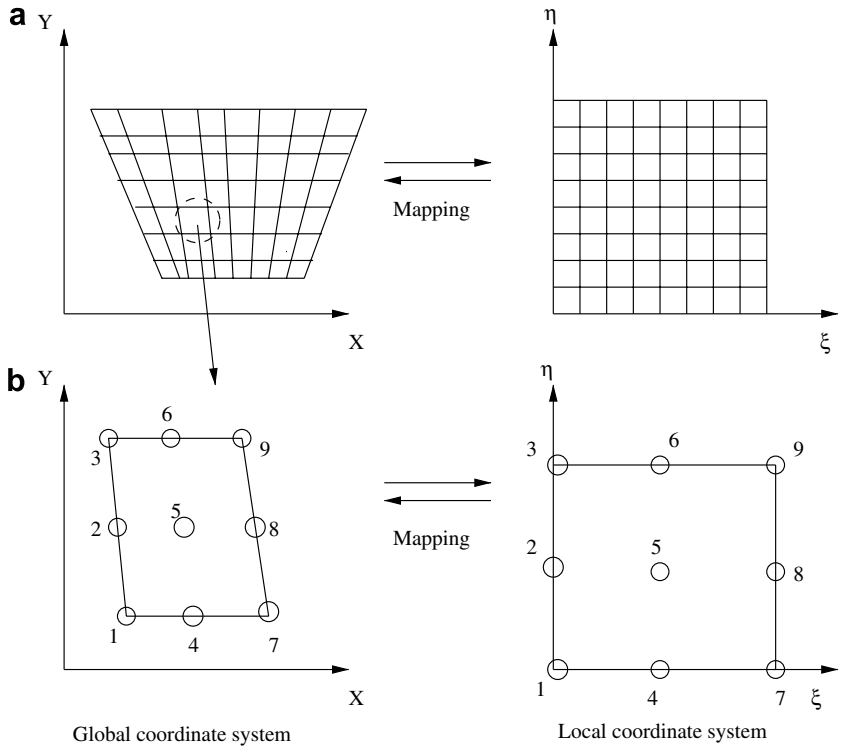

Fig. 11. (a) The mapping of trapezoidal domain to a square domain in ξ–η coordinate system and (b) the mapping of an individual element in ξ–η coordinate system.

is obtained with more than 20 data set. The following correlations are obtained for uniform and non-uniform heating of bottom and side walls.

Cases a and b: uniform heating ($Ra \geqslant 5 \times 10^3$)

$$\begin{aligned}\overline{Nu}_b &= 2.308\,\overline{Nu}_s,\\ &= 1.682\,Ra^{0.11}, \quad Pr = 0.07,\\ &= 0.837\,Ra^{0.201}, \quad Pr = 10.\end{aligned}$$

Cases c and d: non-uniform heating ($Ra \geqslant 3 \times 10^3$)

$$\begin{aligned}\overline{Nu}_b &= 2.308\,\overline{Nu}_s,\\ &= 0.392\,Ra^{0.188}, \quad Pr = 0.07,\\ &= 0.163\,Ra^{0.309}, \quad Pr = 10.\end{aligned}$$

5. Conclusion

In the current investigation the influence of uniform and non-uniform heating of the bottom wall and heat transfer characteristics due to natural convection within a trapezoidal enclosures has been studied in detail. The penalty finite element method helps to obtain smooth solutions in terms of stream function and isotherm contours for uniform and non-uniform heating of the bottom wall with wide ranges of Pr and Ra. We observed that the conduction dominant heat transfer modes for $Ra \leqslant 5 \times 10^3$ during uniform heating of bottom wall whereas the conduction dominant heat transfer is observed for $Ra \leqslant 3 \times 10^3$ for non-uniform heating.

At the onset of convection dominant mode, the temperature contours get compressed towards the side walls and they tend to get deformed towards the upward direction. For $Ra = 10^3$, the circulation inside the enclosure is so weak that the viscous forces are dominant over the buoyancy force. At $Ra = 10^5$, the formation of thermal boundary layers takes place due to the increased circulation intensity. In the case of uniform heating of the bottom wall the heat transfer rate gradually decreases from the left of the bottom wall and attains minimum at the center of the bottom wall and increases to the right. In contrast, for the case of non-uniform heating at $Ra = 10^3$, the heat transfer increases from the left of the bottom wall and attains maximum at the center and then decreases whereas for $Ra = 10^5$ a sinusoidal type of heat transfer rate is obtained. The non-uniform heating exhibits greater heat transfer rates at the center of the bottom wall than with uniform heating case for all Rayleigh number regimes. The local Nusselt number at the side wall is found to be decreased with distance for conduction dominant heat transfer whereas due to highly dense contours near the top portion of the side wall, the local Nusselt number is found to be increased for both uniform and non-uniform heating cases. The average Nusselt number is found to follow power law variation with Rayleigh number for convection dominant regimes. Current work establishes correlations for $Pr = 0.07$ and 10. Liquid metals ($Pr = 0.07$) is used as a coolant in nuclear reactors

for thermodynamic systems and water ($Pr = 10$) is useful in process industries. It may be noted that, current work is based on the angle $\varphi = 30^\circ$. Preliminary investigations have been made with various angles and it has been observed that intensity of circulation increases with increase in φ. It is also observed that multiple circulations gets suppressed as φ increases. Heat transfer coefficient or Nusselt number also been found to vary with φ. A detailed investigation on the influence of φ for circulations and heat transfer rates within trapezoidal cavity is the subject of future research.

Appendix A

The name "isoparametric" derives from the fact that the same parametric function describing the geometry may be used for interpolating spatial variable within an element. Fig. 11 shows a trapezoidal domain mapping to a square domain. The transformation between (x, y) and (ξ, η) coordinates can be defined by $X = \sum_{k=1}^{9} \Phi_k(\xi, \eta) x_k$ and $Y = \sum_{k=1}^{9} \Phi_k(\xi, \eta) y_k$ where (x_k, y_k) are the X, Y coordinates of the k nodal points as seen in Fig. 11a and b and $\Phi_k(\xi, \eta)$ is the basis function. The nine basis functions are:

$$\phi_1 = (1 - 3\xi + 2\xi^2)(1 - 3\eta + 2\eta^2),$$
$$\phi_2 = (1 - 3\xi + 2\xi^2)(4\eta - 4\eta^2),$$
$$\phi_3 = (1 - 3\xi + 2\xi^2)(-\eta + 2\eta^2),$$
$$\phi_4 = (4\xi - 4\xi^2)(1 - 3\eta + 2\eta^2),$$
$$\phi_5 = (4\xi - 4\xi^2)(4\eta - 4\eta^2),$$
$$\phi_6 = (4\xi - 4\xi^2)(-\eta + 2\eta^2),$$
$$\phi_7 = (-\xi + 2\xi^2)(1 - 3\eta + 2\eta^2),$$
$$\phi_8 = (-\xi + 2\xi^2)(4\eta - 4\eta^2),$$
$$\phi_9 = (-\xi + 2\xi^2)(-\eta + 2\eta^2).$$

The above basis functions are used for mapping the trapezoidal domain into square domain and the evaluation of integrals of residuals as given in solution procedure section.

References

[1] I.E. Sarris, I. Lekakis, N.S. Vlachos, Natural convection in a 2D enclosure with sinusoidal upper wall temperature, Numer. Heat Transfer A 42 (2002) 513–530.
[2] A. Bejan, Convection Heat Transfer, 3rd ed., Wiley, Hoboken, NJU, 2004.
[3] B. Gebhart, Buoyancy induced fluid motions characteristics of applications in technology: the 1978 Freeman Scholar Lecture, ASME J. Fluids Eng. 101 (1979) 5–28.
[4] C.J. Hoogendoorn, Natural convection in enclosures, Proceedings of Eighth International Heat Transfer Conference, vol. I, Hemisphere Publishing Corporation, San Francisco, 1986, pp. 111–120.
[5] J. Patterson, J. Imberger, Unsteady natural convection in a rectangular cavity, J. Fluid Mech. 100 (1980) 65–86.
[6] V.F. Nicolette, K.T. Yang, J.R. Lloyd, Transient cooling by natural convection in a two-dimensional square enclosure, Int. J. Heat Mass Transfer 28 (1985) 1721–1732.
[7] J.D. Hall, A. Bejan, J.B. Chaddock, Transient natural convection in a rectangular enclosure with one heated side wall, Int. J. Heat Fluid Flow 9 (1988) 396–404.
[8] J.M. Hyun, J.W. Lee, Numerical solutions of transient natural convection in a square cavity with different sidewall temperature, Int. J. Heat Fluid Flow 10 (1989) 146–151.
[9] T. Fusegi, J.M. Hyun, K. Kuwahara, Natural convection in a differentially heated square cavity with internal heat generation, Numer. Heat Transfer A 21 (1992) 215–229.
[10] J.L. Lage, A. Bejan, The *Ra–Pr* domain of laminar natural convection in an enclosure heated from the side, Numer. Heat Transfer A 19 (1991) 21–41.
[11] J.L. Lage, A. Bejan, The resonance of natural convection in an enclosure heated periodically from the side, Int. J. Heat Mass Transfer 36 (1993) 2027–2038.
[12] C. Xia, J.Y. Murthy, Buoyancy-driven flow transitions in deep cavities heated from below, ASME J. Heat Transfer 124 (2002) 650–659.
[13] L. Iyican, Y. Bayazitoglu, An analytical study of natural convective heat transfer within trapezoidal enclosure, ASME J. Heat Transfer 102 (1980) 640–647.
[14] YU.E. Karyakin, Transient natural convection in prismatic enclosures of arbitrary cross-section, Int. J. Heat Mass Transfer 32 (1989) 1095–1103.
[15] M. Perić, Natural convection in trapezoidal cavities, Numer. Heat Transfer A 24 (1993) 213–219.
[16] R.A. Kuyper, C.J. Hoogendoorn, Laminar natural convection flow in trapezoidal enclosures, Numer. Heat Transfer A 28 (1995) 55–67.
[17] M. Boussaid, A. Djerrada, M. Bouhadef, Thermosolutal transfer within trapezoidal cavity, Numer. Heat Transfer A 43 (2003) 431–448.
[18] J.N. Reddy, An Introduction to the Finite Element Method, McGraw-Hill, New York, 1993.
[19] S. Roy, T. Basak, Finite element analysis of natural convection flows in a square cavity with non-uniformly heated wall(s), Int. J. Eng. Sci. 43 (2005) 668–680.
[20] T. Basak, S. Roy, A.R. Balakrishnan, Effects of thermal boundary conditions on natural convection flows within a square cavity, Int. J. Heat Mass Transfer 49 (2006) 4525–4535.
[21] G.K. Batchelor, An Introduction to Fluid Dynamics, Cambridge University Press, 1993.
[22] M.M. Ganzarolli, L.F. Milanez, Natural convection in rectangular enclosures heated from below and symmetrically cooled from the sides, Int. J. Heat Mass Transfer 38 (1995) 1063–1073.
[23] M. Corcione, Effects of the thermal boundary conditions at the sidewalls upon natural convection in rectangular enclosures heated from below and cooled from above, Int. J. Therm. Sci. 42 (2003) 199–208.